

Excitation of the non-resonant streaming instability around sources of Ultra-High Energy Cosmic Rays

Alessandro Cermenati^{1,2,*}, Roberto Aloisio^{1,2}, Pasquale Blasi^{1,2}, and Carmelo Evoli^{1,2}

¹ Gran Sasso Science Institute (GSSI), Viale Francesco Crispi 7, 67100 L'Aquila, Italy

² INFN-Laboratori Nazionali del Gran Sasso (LNGS), via G. Acitelli 22, 67100 Assergi (AQ), Italy

June 26, 2025

ABSTRACT

Aims. The interpretation of the ultra-high-energy cosmic ray (UHECR) spectrum and composition suggests a suppression of the flux below ~ 1 EeV, as observed by the Pierre Auger Observatory and Telescope Array. A natural explanation for this phenomenon involves magnetic confinement effects. We investigate the possibility that UHECRs self-generate the magnetic turbulence necessary for such confinement via current-driven plasma instabilities.

Methods. Specifically, we show that the electric current produced by escaping UHECRs can excite a non-resonant streaming instability in the surrounding plasma. This instability reduces the diffusion coefficient in the source environment, effectively trapping particles with energies $E \lesssim 0.6 \text{ EeV } \mathcal{L}_{45}^{1/2} R_{\text{Mpc}}^{-1} \lambda_{10}^2$ for times exceeding the age of the Universe. Here, \mathcal{L}_{45} is the source luminosity in units of 10^{45} erg/s , R_{Mpc} is the radial size in Mpc, and λ_{10} is the intergalactic magnetic field coherence length in units of 10 Mpc. Here we discuss in detail the conditions, in terms of source luminosity, initial magnetic field, and the environment in which this complex phenomenon occurs, that need to be fulfilled in order for self-confinement to take place near a source of UHECRs, and the caveats that affect our conclusions. We emphasize that these conclusions are derived within a simplified model framework; their wider applicability requires that the assumptions hold in realistic source environments.

Results. By modeling a population of UHECR sources with a luminosity function typical of extragalactic gamma-ray sources, we connect the spectrum of escaping particles to the luminosity distribution. Furthermore, we calculate the contribution of these confined particles to cosmogenic neutrino production, finding consistency with current observational constraints. Our results suggest that self-induced turbulence may play an important role in shaping the UHECR spectrum and, in particular, may account for the flux suppression near their sources, offering a promising framework for interpreting current observations.

Key words. Astroparticle physics – Cosmic rays – Neutrinos

1. Introduction

The observed spectrum and composition of ultra-high-energy cosmic rays (UHECRs), as measured by the Pierre Auger Observatory (Auger) (Abreu et al. 2021; Aab et al. 2020), provide invaluable insights into their origin. The distribution of the depth of shower maximum (X_{max}) (Aab et al. 2014; Aab et al. 2014; Aab et al. 2016) reveals information about primary particle types, while spectrum fits, accounting for source evolution and propagation effects (Aab et al. 2017; Abdul Halim et al. 2023), constrain key source parameters such as the spectral shape and elemental composition.

Several robust conclusions have emerged from these fits:

- 1) Above the second knee, UHECRs transition from a mix of protons and medium-mass nuclei (e.g., nitrogen) to a predominantly mixed composition near the ankle ($\sim 10^{18.3} \text{ eV}$),
- 2) At energies $\gtrsim 10^{19} \text{ eV}$, the absence of a light component implies that the maximum rigidity of sources is limited to $R \lesssim 10^{19} \text{ V}$, relaxing the demands in terms of acceleration models (Bergman 2006; Shinozaki & Teshima 2004);
- 3) The inferred source spectrum is unusually hard, with slopes $\gamma \lesssim 1$, a result inconsistent with the $\gamma \gtrsim 2$ expected from standard acceleration models such as diffusive shock acceleration at non-relativistic and relativistic shocks (Blandford & Ostriker 1978; Blandford & Eichler 1987; Sironi et al. 2015). Although

unusual, such hard spectra have been found in some acceleration models, such as rapidly spinning neutron stars (Blasi et al. 2000; Arons 2003; Kotera et al. 2015), second-order stochastic acceleration in gamma-ray bursts (Asano & Mészáros 2016), and reconnection events in relativistic plasmas (Zhang et al. 2023). More recent Auger data analyses even suggest inverted source spectra ($\gamma < 0$) above the ankle, introducing a tension with existing astrophysical models (Abdul Halim et al. 2023). Furthermore, to reproduce observables below the ankle, an additional soft-spectrum component ($\gamma \sim 3.5$) is needed, consistent with measurements of the proton spectrum by KASCADE-Grande (Kang 2023) and IceTop (Aartsen et al. 2019).

A natural interpretation of these findings invokes confinement of UHECRs with energies below the ankle, a scenario that can be realized in two main classes of models: 1) Confinement around the sources: In this scenario, heavy nuclei experience energy-dependent confinement in the source vicinity or even inside the source. Their prolonged residence time enhances photo-disintegration processes, altering the observed composition and spectrum (Unger et al. 2015; Muzio et al. 2022); 2) Magnetic Horizon Effect: Here, the delayed arrival of low-energy particles is attributed to diffusion in strong extragalactic magnetic fields ($\gtrsim 10 \text{ nG}$). This results in an effective low-energy cut-off, dependent on the strength and structure of the intergalactic magnetic field (Aloisio & Berezhinsky 2004; Mollerach & Roulet 2013; Abdul Halim et al. 2024). Both models require specific

* alessandro.cermenati@gssi.it

assumptions about the source environment or the intergalactic magnetic field (IGMF). In particular, the latter demands field strengths near observational upper limits imposed by radio synchrotron and Faraday rotation measurements (Amaral et al. 2021; Carretti et al. 2022).

A third possibility, originally proposed in Blasi et al. (2015), involves the generation of self-induced turbulence. The electric current carried by escaping UHECRs drives a non-resonant streaming instability (Bell 2004; Amato & Blasi 2009), which amplifies small-scale magnetic perturbations. These perturbations grow non-linearly, saturating at scales comparable to the gyroradius of the dominant particles in the current. This mechanism modifies UHECR transport near the source, effectively confining particles and regulating their escape. Notably, Blasi et al. (2015) demonstrated that for a source luminosity of $\mathcal{L} \sim 10^{44}$ erg/s, this self-confinement mechanism can trap sub-EeV particles for timescales exceeding the typical source lifetime of ~ 10 Gyr.

In this work, we build upon this last model and explore four critical aspects: 1) we investigate the minimum luminosity required for a UHECR source to induce a low-energy cut-off via self-confinement in the EeV energy range, as a function of the source parameters. Here, the term *source* refers to the astrophysical object hosting the accelerator rather than the accelerator itself. For example, if gamma-ray bursts serve as the acceleration sites within a galaxy, the source in our context would be the galaxy. This distinction emphasizes the fact that it is the transport of UHECRs within the environment surrounding the astrophysical host, rather than around the acceleration region, that governs self-confinement. 2) We consider the advection of UHECRs with the background plasma, set in motion due to the accumulation of cosmic rays, following the approach outlined in Blasi & Amato (2019). Specifically, we find that the strong coupling between cosmic rays and the background plasma, driven by self-generated magnetic perturbations, imposes an upper limit on the current of particles escaping the source. Consequently, at sufficiently high source luminosities, the drift velocity of the plasma, assumed to be of the same order of magnitude as the Alfvén speed in the amplified magnetic field, becomes large enough to carry particles outside the confinement region on a timescale shorter than the source lifetime. 3) We review the constraints on the pre-existing magnetic field required for the growth of the non-resonant streaming instability (Zweibel & Everett 2010). If the initial magnetic field is too strong, the non-resonant branch of the instability is suppressed. Conversely, if the field is too weak, the perturbations are induced on a scale comparable with the Larmor radius of background plasma protons, limiting the growth of the instability. The latter condition depends on the energy of the particles driving the current and generating the perturbations. However, this limitation is not severe if additional types of magnetic turbulence within the source suppress the escape of particles with energies \lesssim PeV into the IGM. As previously noted, the source in this context refers to the astrophysical object hosting the accelerator, such as a galaxy or galaxy cluster, and thus the escape of low-energy particles can be regulated by turbulence not considered in this study. 4) As in these models, the source spectrum exhibits a non-linear dependence on source luminosity. We then model the escape of UHECRs from a population of putative sources with a specified luminosity function (Ajello et al. 2009; Burlon et al. 2011; Ajello et al. 2012; Qu et al. 2019) to investigate how this distribution impacts the observed spectrum at Earth. Notably, when self-generation effects are active, the spectrum of cosmic rays escaping the sources becomes nearly independent of the spectral

shape at the acceleration site. Instead, the slope of the spectrum below the break depends on the shape of the source luminosity function.

Finally, we estimate the neutrino flux from confined protons near the source and compare it to the flux from escaping protons. Even under optimistic assumptions, we find that the confinement-dominated regions produce signals consistent with current observational limits (Kopper 2017; Abbasi et al. 2025).

While this work focuses on protons to highlight the self-confinement mechanism, the results are rigidity-dependent and extendable to mixed compositions, as required by UHECR observations (Abdul Halim et al. 2023). A detailed analysis of the implications of this model for the mass composition will be carried out in a forthcoming publication.

2. Model

2.1. Excitation of the Non-Resonant Streaming Instability Around UHECR Sources

The physical setup adopted here is similar to the one first introduced in Refs. Blasi et al. (2015); Blasi & Amato (2019): the source is assumed to have a typical radius R and be located in a region in which a pre-existing turbulent magnetic field B_0 is present, with a typical coherence scale λ_B . UHECRs escaping the source gyrate around the direction of the local magnetic field and can be considered magnetized or unmagnetized depending on whether their gyroradius is smaller or larger than λ_B , respectively. For magnetized particles, we can safely assume that the guiding center follows the magnetic field line for at least a distance $\sim \lambda_B$ from the source, since under rather generic conditions on such scales, perpendicular diffusion is less relevant. We also assume that the differential spectrum of particles released into the surrounding medium is $\propto E^{-2}$ between a minimum (E_{min}) and maximum (E_{max}) energy. In this simplified picture, the number density of particles with energy larger than E in the flux tube of length λ_B can be written as

$$n_{CR}(> E) = \frac{2\mathcal{L}_p E^{-1}}{c\Lambda\pi R_c^2(E)}, \quad (1)$$

where \mathcal{L}_p is the *proton* luminosity of the source, $\Lambda = \ln\left(\frac{E_{max}}{E_{min}}\right) \approx 20$ serves as a normalization factor, and $R_c(E) = R_L(E) + R$, with $R_L(E)$ being the Larmor radius of particles in the pre-existing magnetic field. Clearly, this expression relies on the assumption that the motion of the particles is approximately ballistic, with velocity $\sim c/2$, in the flux tube, as it is supposed to be in the absence of an appreciable level of magnetic perturbations. The introduction of $R_c(E)$ mimics the fact that the particles injected by the source are distributed on a transverse surface that is the largest between the size of the source, R , and the Larmor radius of the same particles in the pre-existing IGMF B_0 . For reference values $B_0 = 1$ nG and $\lambda_B = 10$ Mpc, the transition from magnetized and unmagnetized particles occurs at ~ 10 EeV. We assume $R \sim 1$ Mpc as a fiducial value of the source radius, but it is useful to keep in mind that this size may be appreciably smaller. Under these conditions, the size of the flux tube turns out to be roughly energy independent for energies $\lesssim 1$ EeV. It is worth noting that for these reference values of the parameters, an interesting phenomenology is expected to appear at the same energy where, based on the Auger data, one would expect the maximum energy of protons, mainly constrained by the mass composition at higher energies (Abdul Halim et al. 2023).

UHECRs escaping the source create a positive electric current density $J_{\text{CR}}(> E) = e \frac{c}{2} n_{\text{CR}}(> E)$, which may excite a non-resonant streaming instability provided the energy density carried by the current is larger than the magnetic energy density in the pre-existing field (Bell 2004):

$$\frac{E J_{\text{CR}}(> E)}{ec} \gtrsim \frac{B_0^2}{4\pi} \rightarrow \frac{\mathcal{L}_p}{c \Lambda \pi R_c^2(E)} \gtrsim \frac{B_0^2}{4\pi}. \quad (2)$$

In the linear stage of the growth of the non-resonant instability, the modes that grow are quasi-purely growing at large wavenumbers. The maximum growth occurs at

$$k_{\text{max}} = \frac{4\pi}{c} \frac{J_{\text{CR}}(> E)}{B_0} \gg \frac{1}{R_L(E)}, \quad (3)$$

and the corresponding growth rate is

$$\gamma_{\text{max}}(E) = v_A k_{\text{max}} \simeq \frac{2}{\sqrt{\pi n_b m_p}} \frac{e \mathcal{L}_p}{c \Lambda R^2 E}, \quad (4)$$

where $v_A = B_0 / \sqrt{4\pi n_b m_p}$ represents the Alfvén speed in the surrounding magnetic field, and n_b is the number density of the medium through which the cosmic rays propagate, which we assume to be of the order of the mean cosmological baryon density. Notice that, based on Equation (4), the maximum growth rate is independent of the initial value of the local magnetic field, B_0 .

In order for the instability to be excited, as discussed above, the condition in Eq. (2) must be fulfilled. This condition translates into an upper limit on the strength of the IGMF:

$$B_0 \lesssim B_{\text{upper}} = \sqrt{\frac{4\mathcal{L}_p}{\Lambda R^2 c}} \approx 25 \text{ nG} \left(\frac{\mathcal{L}_p}{10^{45} \text{ erg/s}} \right)^{1/2} \left(\frac{R}{\text{Mpc}} \right)^{-1}. \quad (5)$$

Since the perturbations grow on small scales compared to the gyroradius of the particles dominating the current, particle transport is only weakly perturbed during this stage, and in fact, the magnetic field perturbations δB on a scale $\sim k_{\text{max}}^{-1}$ can grow to values $\delta B / B_0 \gg 1$. At later stages, the $\mathbf{J} \times \mathbf{B}$ force, perpendicular to B_0 , stretches the perturbations on larger scales. Eventually, the current becomes affected by the growth of the perturbations and the instability saturates, when $\delta B = \delta B_{\text{sat}} \sim B_{\text{upper}}$. Numerical simulations suggest that the time required for this saturation to be achieved requires ~ 5 – 10 e-folds (Gargaté et al. 2010), which translates into a saturation time:

$$\tau_{\text{sat}}(E) \sim 5 \gamma_{\text{max}}^{-1}(E) \approx 2 \text{ Gyr} \left(\frac{\mathcal{L}_p}{10^{45} \text{ erg/s}} \right)^{-1} \left(\frac{R}{\text{Mpc}} \right)^2 \left(\frac{E}{\text{EeV}} \right). \quad (6)$$

One should appreciate that, for UHECR with $E \lesssim \text{EeV}$, the self-generated magnetic field reaches its saturation level δB_{sat} in a time much smaller than the duration of the source activity, $t_{\text{age}} \sim 10 \text{ Gyr}$. We stress once more that by source here we mean the astrophysical object from which UHECRs are escaping. Hence, the source duration can be reasonably assumed as comparable to the age of the universe, and \mathcal{L}_p as the effective average luminosity.

As first discussed in Zweibel & Everett (2010), the growth of the non-resonant instability depends on small-scale physics that is often overlooked. For our purposes, since $k_{\text{max}} R_L \gg 1$, it may happen that k_{max}^{-1} becomes comparable with the Larmor radius of thermal ions, $R_{L,\text{th}}$. The condition $k_{\text{max}} R_{L,\text{th}} \lesssim 1$ translates into a lower limit on the pre-existing IGMF:

$$B_0 > B_{\text{lower}} = \left(\frac{16 \mathcal{L}_p^2 m_p k_B T_{\text{IGM}}}{\Lambda^2 E_{\text{min}}^2 R^4} \right)^{1/4} \\ \approx 10^{-4} \text{ nG} \left(\frac{\mathcal{L}_p}{10^{45} \text{ erg/s}} \right)^{1/2} \left(\frac{T_{\text{IGM}}}{10^4 \text{ K}} \right)^{1/4} \left(\frac{R}{\text{Mpc}} \right)^{-1} \left(\frac{E_{\text{min}}}{\text{PeV}} \right)^{-1/2}. \quad (7)$$

This bound is somewhat dependent upon the minimum energy of the particles that manage to reach the location where the growth rate is being estimated. The reference value shown in Eq. (7) is obtained by assuming that particles with energy $\gtrsim 1 \text{ PeV}$ reach a given location. It is highly non-trivial to assess this point: low-energy particles, well below the PeV range, may be potentially scattered by any type of small-scale turbulence, making it difficult to build a completely self-consistent picture. However, one could argue that it is highly unlikely for very low-energy particles to move quickly to large distances from the source, possibly due to other less effective instabilities (such as the resonant streaming instability, which is slower but still present). We will use the estimate in Eq. (7) as a warning to keep in mind when drawing conclusions concerning our model.

In summary, if the IGMF lies within the range that supports the growth of the non-resonant instability, then within a timescale of order τ_{sat} , the transport of UHECRs will be substantially altered by the emergence of a Bohm-like diffusion coefficient, which can be approximated as:

$$D = \frac{c}{3} \frac{E}{e \delta B_{\text{sat}}} \approx 4 \frac{\text{Mpc}^2}{\text{Gyr}} \left(\frac{\mathcal{L}_p}{10^{45} \text{ erg/s}} \right)^{-1/2} \left(\frac{R}{\text{Mpc}} \right) \left(\frac{E}{\text{EeV}} \right). \quad (8)$$

As a consequence, for sufficiently low energies, the diffusion time out of the flux tube, characterized by a length scale λ_B , can easily exceed the age of the universe. This behavior will be modeled in detail in the next section.

The fact that diffusion becomes very effective implies that cosmic rays are bound to the plasma and eventually follow the plasma motion. Moreover, the accumulation of cosmic rays near the source leads to large pressure gradients that set the background plasma in motion. This phenomenon was discussed in some detail in Blasi & Amato (2019), where the authors provide an order of magnitude of the force exerted on the plasma and speculate that the plasma is set in motion with a velocity that is expected to be of the same order of magnitude as the Alfvén speed in the amplified field, where the field is argued to reach saturation primarily because of the Lorentz force reaction on the background plasma (Bell 2004), rather than due to the bulk motion of the plasma itself (Riquelme & Spitkovsky 2009).

Following the same line of thought as in Blasi & Amato (2019), we assume that the plasma motion occurs with the Alfvén speed in the amplified field:

$$V_A \approx \frac{\delta B_{\text{sat}}}{\sqrt{4\pi m_p n_b}} \sim 0.1 \frac{\text{Mpc}}{\text{Gyr}} \left(\frac{\mathcal{L}_p}{10^{45} \text{ erg/s}} \right)^{1/2} \left(\frac{R}{\text{Mpc}} \right)^{-1}, \quad (9)$$

and that cosmic rays are advected away from the source at about the same speed.

It is worth emphasizing that the displacement of the background plasma due to cosmic ray pressure gradients is not unexpected: it is in fact observed in hybrid-PIC simulations of the escape of particles from a source (e.g. a SNR) (Schroer et al. 2022, 2021) although in a different, less extreme, range of values of the relevant parameters. These simulations show that not only the plasma is set in motion in the direction of the local magnetic field, but also a cavity is excavated in such a plasma in the transverse direction. The plasma motion appears to occur at a speed comparable to the Alfvén speed in the amplified field.

2.2. UHECR Transport in the IGM

The non-linear chain of phenomena responsible for the excitation, growth, and saturation of the non-resonant instability, as

well as the transport of cosmic rays in the self-generated perturbations, is extremely complex and poses a serious challenge not only from the computational point of view but from the conceptual point of view as well. For instance, after a time $\tau_{\text{sat}}(E)$, particles with energy E are expected to be slowed down considerably, making their motion no longer ballistic. Consequently, one might argue that the previously proposed calculation of the current becomes inappropriate. However, as discussed in Blasi & Amato (2019), while self-confinement makes transport diffusive, the current in the region where particles are confined remains unchanged at the lowest order: the current is conserved, but limited to a smaller region around the source, which is the reason why particles are confined and gradually leak outwards, provided there is sufficient time.

Another complication arises from the fact that confinement causes the flux tube where UHECRs are confined to become over-pressured relative to the surrounding medium, so that the tube is expected to inflate a bubble, expanding at roughly the Alfvén speed (Schroer et al. 2021, 2022). Given the relatively low value of such speed compared to the drift velocity of UHECRs due to diffusion, here we neglect this phenomenon as well, although it may become important in the lower energy region, where transport becomes dominated by advection.

Given the paramount conceptual complexity of this scenario, here we treat the escape of UHECRs from the source vicinity in a very simple but physically motivated way: the spectrum of the escaping particles is the same as that injected by the source for those energies for which the escape time is shorter than t_{age} and vanishes otherwise. We define the escape time from the near-source region as follows:

$$\tau_{\text{esc}}(E) = \left(\frac{1}{\tau_{\text{adv}}} + \frac{1}{\tau_{\text{diff}}(E)} \right)^{-1}, \quad (10)$$

where $\tau_{\text{adv}} \sim \frac{\lambda_B}{V_A}$ and $\tau_{\text{diff}}(E) \sim \frac{\lambda_B^2}{4D(E)}$ are the advective and diffusive timescale, respectively. These time scales are shown in Fig. 1a for $\lambda_B = 10$ Mpc, $t_{\text{age}} = 10$ Gyr, and different values of the source luminosity.

Although the diffusion coefficient is expected to be Bohm-like (Eq. (8)), at sufficiently high energy, the time required for the saturation of the non-resonant instability, $\tau_{\text{sat}}(E)$, will exceed t_{age} . In this case, there will not be enough time for the generation of power on the resonant scale. Consequently, such particles will undergo small pitch angle scattering with a typical diffusion coefficient $D(E) \propto E^2$ (Subedi et al. 2017). To account for this effect, we write the diffusion coefficient in the following generalized form:

$$D = \frac{c}{3} \left(\frac{E_c}{e\delta B} \right) \left[\left(\frac{E}{E_c} \right) + \left(\frac{E}{E_c} \right)^2 \right], \quad (11)$$

where E_c is defined by the condition $\tau_{\text{sat}}(E) = t_{\text{age}}$. Depending on specific parameters, E_c is in the range $\approx (0.1-1)$ EeV.

Moreover, when the particle energy becomes large enough that the gyration radius exceeds the size R of the source, the effective cross-section of the flux tube increases as E^2 , and it becomes much harder to excite the non-resonant instability. This occurs when $E \gtrsim E_R$, where $E_R \approx eB_0 R \approx \text{EeV } B_{\text{nG}} R_{\text{Mpc}}$. Finally, when particles cease to be magnetized on a scale λ_B , namely when $E \gtrsim E_M$ with $E_M = eB_0 \lambda_B \approx 10 \text{ EeV } B_{\text{nG}} \lambda_{10}$, the escape of the particles becomes quasi-ballistic and the effect of self-generation does not take place. If the pre-existing magnetic field is on the order of ~ 1 nG, this is not too much of a concern since the range of energies where this occurs is close to or even in

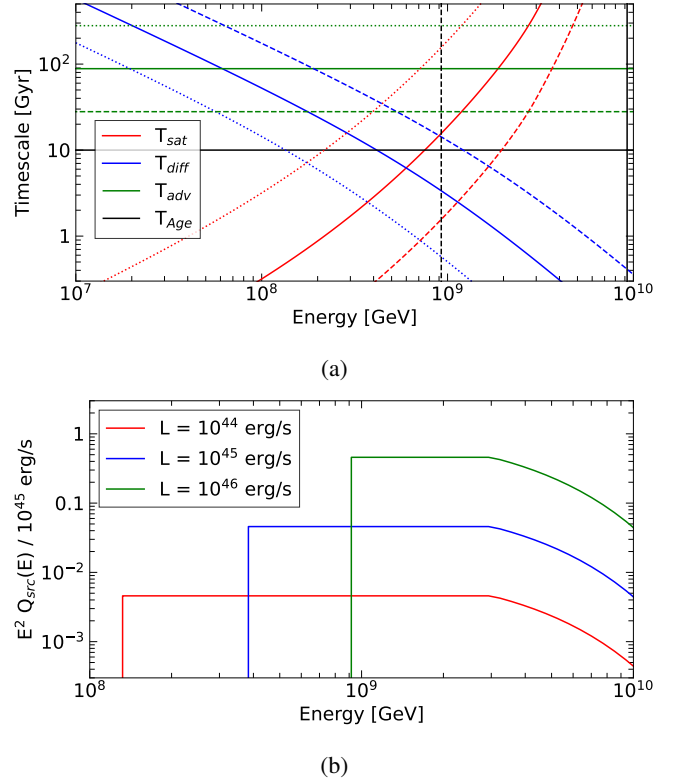


Fig. 1: Top panel: Relevant timescales for $\mathcal{L}_p = 10^{44}$ erg/s (dotted), 10^{45} erg/s (solid), and 10^{46} erg/s (dashed). The vertical lines show the critical energies defined by $R_L(E) = R$ (dashed) and $R_L(E) = \lambda_B$ (solid). Bottom panel: Cosmic rays injection (Eq. (15)) at $t_{\text{age}} = 10$ Gyr for $\mathcal{L}_p = 10^{44}$ erg/s (red), 10^{45} erg/s (blue), and 10^{46} erg/s (green).

excess of the maximum energy of the protons compatible with the measured mass composition, namely a few EeV. However, for smaller strengths of the IGMF and if the coherence scale λ_B is much smaller than 10 Mpc, this becomes a serious blow in that the propagation of particles in the range $\lesssim 1$ EeV becomes ballistic, and the low energy suppression disappears. Hence, to be on the safe side, the model discussed here requires the IGMF to be in the \lesssim nG range, with $\lambda_B \gtrsim 10$ Mpc, for the non-resonant instability to be of phenomenological relevance in the EeV energy range.

Provided these conditions are satisfied, the requirement that the instability is excited (Eq. (5)) translates into a minimum source luminosity in the form of cosmic rays:

$$\mathcal{L}_p \gtrsim \mathcal{L}_{\text{min}} \approx 10^{42} \text{ erg/s} \left(\frac{B_0}{1 \text{ nG}} \right)^2 \left(\frac{R}{1 \text{ Mpc}} \right)^2. \quad (12)$$

It is worth noting that the Alfvén speed in the amplified field increases with the amplified magnetic field, which typically happens when the source luminosity is higher. This increase would reduce the advection time, which may eventually become too short in the EeV range to guarantee CR confinement. The condition that the advection time exceeds the source age, $V_A t_{\text{age}} \gtrsim \lambda_B$, sets an upper limit on the source luminosity for which the considerations discussed here apply:

$$\mathcal{L}_p \lesssim \mathcal{L}_{\text{max}} \approx 10^{47} \frac{\text{erg}}{\text{s}} \left(\frac{\lambda_B}{10 \text{ Mpc}} \right)^2 \left(\frac{R}{1 \text{ Mpc}} \right)^2. \quad (13)$$

For typical values of the parameters, this upper limit does not pose a severe concern for the applicability of our calculations.

When the source luminosity is within the range bounded by the values set by Equations (12) and (13), cosmic ray confinement near the source occurs if the diffusion time exceeds the source age. This phenomenon results in a *cutoff* in the spectrum of UHECRs released into the IGM at energies below

$$E_D \simeq 0.6 \text{ EeV} \left(\frac{\mathcal{L}_p}{10^{45} \text{ erg/s}} \right)^{1/2} \left(\frac{R}{\text{Mpc}} \right)^{-1} \left(\frac{\lambda_B}{10 \text{ Mpc}} \right)^2. \quad (14)$$

Modeling the exact shape of this cutoff is beyond the scope of this work and it would not significantly alter the conclusions. Instead, we adopt a simple yet effective approach that captures the essential physics of the problem. In this context, we model the released spectrum of the source as:

$$Q_{\text{src}}(E, \mathcal{L}_p) = q(E) \mathcal{H} [t_{\text{age}} - \tau_{\text{esc}}(E, \mathcal{L}_p)], \quad (15)$$

where $q(E) = \frac{\mathcal{L}_p E^{-2}}{\Lambda}$, and the Heaviside function \mathcal{H} ensures that particles with escape times longer than the source age remain confined within the source. The shape of the spectrum of escaping particles from the near-source region is shown in Fig. 1b for three values of the source luminosity, normalized to $E_{\text{min}} = 1 \text{ GeV}$, and for our reference values of the environmental parameters, $R = 1 \text{ Mpc}$, $\lambda_B = 10 \text{ Mpc}$, $B_0 = 1 \text{ nG}$ and $E_{\text{max}} = 3 \text{ EeV}$.

3. Results

3.1. Emissivity from a population of non-identical sources

As discussed in the previous section, the spectrum of a source that is actually released into the IGM depends in a non-linear way upon the source luminosity. Therefore, it is interesting to explore what happens when a luminosity function $\Phi(\mathcal{L}_p, z)$ is assumed for the putative source population. The case of identical sources with a single value of the luminosity, usually adopted in the literature on the origin of UHECRs for simplicity (see for instance Abdul Halim et al. 2023), can be recovered by restricting the luminosity function to a narrow range.

The emissivity in the form of protons as a function of energy at a given redshift can be easily calculated as:

$$Q_p(E, z) = \int_{\mathcal{L}_{\text{low}}}^{\mathcal{L}_{\text{high}}} d\mathcal{L}_p \Phi(\mathcal{L}_p, z) Q_{\text{src}}(E, \mathcal{L}_p), \quad (16)$$

where \mathcal{L}_{low} and $\mathcal{L}_{\text{high}}$ identify the minimum and maximum luminosity for which the luminosity function applies.

The simplest choice of a luminosity function, useful to clarify some points, is a power law distribution:

$$\Phi_{\text{PL}}(\mathcal{L}_p, z) = \frac{dN}{d\mathcal{L}_p dV} = A \times \begin{cases} \left(\frac{\mathcal{L}_p}{\mathcal{L}_{\text{low}}} \right)^{-\beta} & \text{if } \mathcal{L}_{\text{low}} < \mathcal{L}_p < \mathcal{L}_{\text{high}} \\ 0 & \text{otherwise,} \end{cases} \quad (17)$$

where V is the comoving volume and A is a normalization constant with units of $\text{Mpc}^{-3} \text{ erg}^{-1} \text{ s}$.

The emissivity in the form of protons, given a power law luminosity function, is shown in Figure 2. In the left panel, the results for $\beta = 1$ are presented for three different values of $\mathcal{L}_{\text{high}}$, as indicated. Notice that for $\beta < 2$, the emissivity at a given energy is dominated by the luminosity region near $\mathcal{L}_{\text{high}}$, which

is the reason why in the left panel we only change the value of $\mathcal{L}_{\text{high}}$. The suppression of the flux of protons injected at low energies is easily identifiable and is due to the self-confinement of UHECR near the sources. The suppression is not as sharp as the one in Figure 1 as a result of the convolution of different source luminosities. For $\beta < 2$, it can be easily shown that the energy dependence of the emissivity for self-confined particles is approximately $Q(E) \propto E^{-2+2(2-\beta)}$. This mimics a source spectrum that is harder than the canonical E^{-2} , although this shape does not directly relate to the acceleration process, as discussed earlier. The drop in the emissivity for energies $\gtrsim 3 \text{ EeV}$ is due to a cutoff in the source spectrum at that energy, required to fit the Auger data as found in previous phenomenological descriptions (see for instance Aloisio & Berezhinsky 2004; Abdul Halim et al. 2023). The curve corresponding to $\mathcal{L}_{\text{high}} = 10^{47} \text{ erg/s}$ shows a plateau at low energies (no suppression). This case highlights the role of advection: for high source luminosities, the CR current is so intense that the diffusion coefficient becomes very small, causing particles to escape due to advection with the self-generated perturbations. This case has been shown only as an illustration of the role of advection, but sources with such a high CR luminosity may imply a possibly unrealistic total luminosity of the sources, at least when averaged over a time $t_{\text{age}} \sim 10 \text{ Gyr}$.

In the central panel of Figure 2, we present the emissivity for $\mathcal{L}_{\text{low}} = 10^{42} \text{ erg/s}$ and $\mathcal{L}_{\text{high}} = 10^{46} \text{ erg/s}$, with three values of β . For $\beta = 1$, there is a noticeable flux suppression for $E \lesssim 0.5 \text{ EeV}$, as discussed previously. In the case of $\beta = 2.5 (> 2)$, the main contribution to the emissivity is provided by low luminosity sources, for which the self-confinement is limited to lower energy CRs, as illustrated by the green curve in the central panel of Figure 2. Given the small value of \mathcal{L}_{low} , the suppression occurs at exceedingly low energies, approximately 10 PeV .

Finally, in the right panel of Figure 2, we show the emissivity in the form of protons for $\beta = 1$ and different values of \mathcal{L}_{low} , while $\mathcal{L}_{\text{high}}$ is fixed to the value of 10^{46} erg/s . As in the previous cases, the high energy suppression is due to the adoption of an exponential cutoff at 3 EeV . Higher values of \mathcal{L}_{low} result in a more pronounced suppression of the emissivity at higher energies compared to lower \mathcal{L}_{low} values. As a consequence, the region of hardening in the emissivity, due to the convolution with the luminosity function, extends to a narrower energy region when \mathcal{L}_{low} increases. Nonetheless, in all scenarios, the effect of self-confinement, together with the convolution with a luminosity function, leads to mimicking a hard injection spectrum, again unrelated to the intrinsic spectrum of accelerated particles.

The case of a simple power-law luminosity function, as illustrated above, provides useful insights into the expected effects: luminous sources cause self-confinement of UHECRs that extends to higher energies, and the convolution with a luminosity function, for $\beta < 2$, leads to a hardening below the energy for which confinement is caused by sources with luminosity around $\mathcal{L}_{\text{high}}$. In this energy range, the spectrum behaves as $Q(E) \propto E^{-2+2(2-\beta)}$. For $\beta > 2$, the confinement is dominated by the sources with the lowest luminosity.

Although this case may be sufficient to support the physical picture that we are interested in, since in many cases the luminosity function is modeled as a broken power law, for instance in the cases of AGN and Starburst Galaxies as sources or astrophysical objects hosting the sources, we briefly discuss this scenario using the following functional form for the luminosity function:

$$\Phi(\mathcal{L}_p, z) = \frac{dN}{d\mathcal{L}_p dV} = \frac{Ae(z)}{\log(10)\mathcal{L}_p} \left[\left(\frac{\mathcal{L}_p}{\mathcal{L}_*} \right)^{\gamma_1} + \left(\frac{\mathcal{L}_p}{\mathcal{L}_*} \right)^{\gamma_2} \right]^{-1}, \quad (18)$$

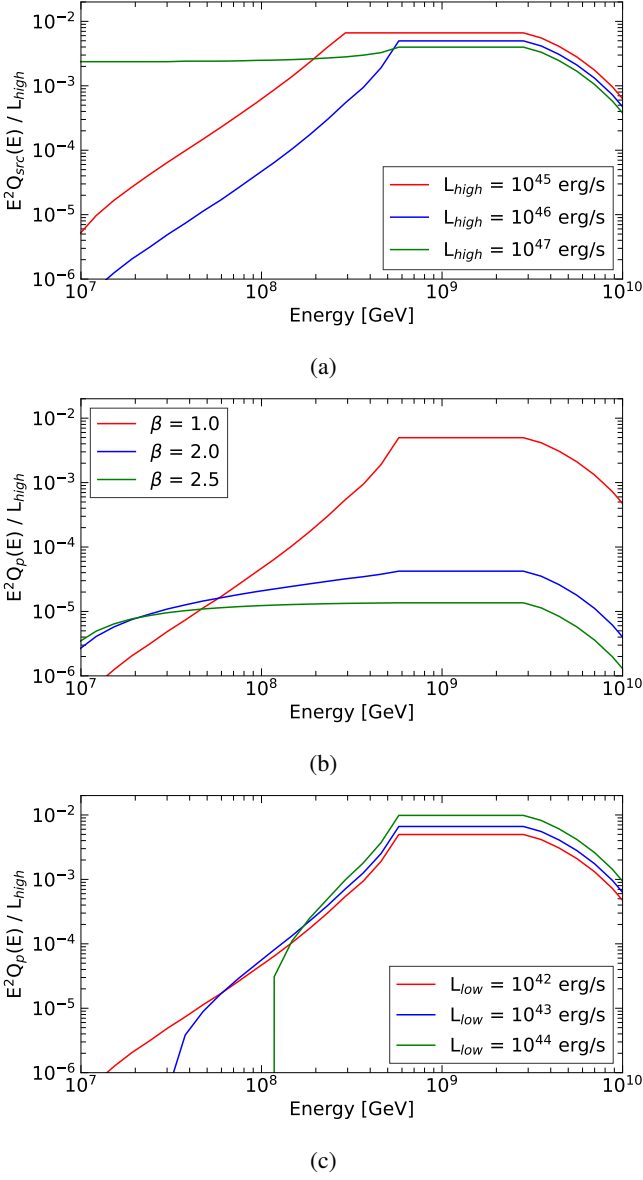


Fig. 2: Proton emissivity calculated from Eq. (16), considering a simple power law Luminosity Function. Top panel: different choices of $\mathcal{L}_{\text{high}}$, with $\beta = 1$ and $\mathcal{L}_{\text{low}} = 10^{42}$ erg/s. Central panel: different choices of β , with $\mathcal{L}_{\text{low}} = 10^{42}$ erg/s and $\mathcal{L}_{\text{high}} = 10^{46}$ erg/s. Bottom panel: different choices of \mathcal{L}_{low} , with $\beta = 1$ and $\mathcal{L}_{\text{high}} = 10^{46}$ erg/s.

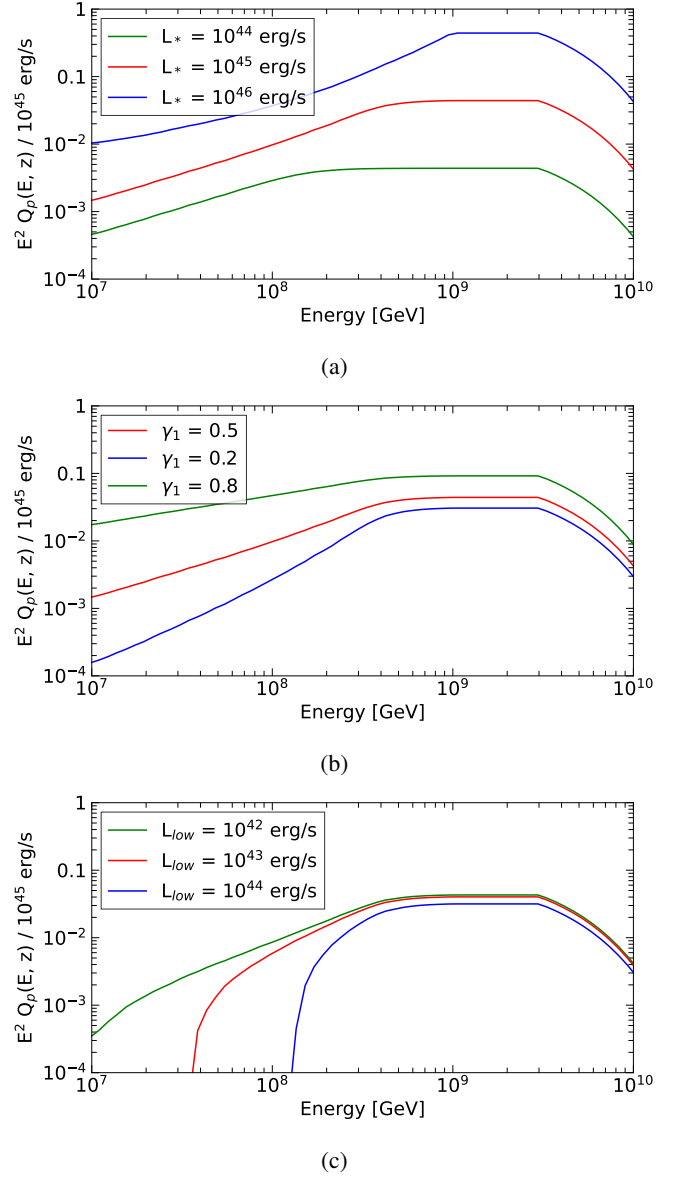


Fig. 3: Proton emissivity calculated from Eq. (16), considering a broken power law Luminosity Function (Eq. (18)) with $\gamma_2 = 2.5$. Top panel: different positioning of \mathcal{L}_* ; the low luminosity index is $\gamma_1 = 0.5$. Central panel: different low luminosity behavior; the positioning of the break is fixed at $\mathcal{L}_* = 10^{45}$ erg/s. Bottom panel: different choices of \mathcal{L}_{low} ; the position of the break is $\mathcal{L}_* = 10^{45}$ erg/s and the slope is $\gamma_1 = 0.5$.

where V is the comoving volume, γ_i are the slopes characterizing the low and high-luminosity behavior, \mathcal{L}_* is a break luminosity, and A is a normalization constant. The term $e(z)$ can be chosen to model the redshift evolution of the luminosity function, which varies with the source population. Here, for simplicity and for the sole purpose of illustrating the physical results, we adopt a constant redshift evolution $e(z) = 1$ up to $z_{\text{max}} = 3$. A more detailed review of the luminosity distribution modeling for galaxies and AGN-like objects can be found in Fotopoulou, S. et al. (2016). As in the previous case, the emissivity in the form of protons can be computed using Equation (16). We show our results in Figure 3 for different choices on the parameters defining the luminosity function.

Given the wide variety of possible choices of the values of the parameters, we try to find guidance in the luminosity function for some sources, such as that of AGN-like sources, for which typically values of $\gamma_1 \lesssim 1$ and $\gamma_2 \gtrsim 2$ are fitted in the X-ray (Ajello et al. 2009; Burlon et al. 2011) and γ -ray (Ajello et al. 2012; Qu et al. 2019) bands. Based on the results found in the cases of a power law luminosity function, it is clear that most results of physical relevance will be determined by the choice of γ_1 and \mathcal{L}_* . Therefore, we fix $\gamma_2 = 2.5$ and briefly comment on the dependence of the results on the other parameters. Again, we can use our findings in the power law case as guidance: most of our previous conclusions still hold when the role of $\mathcal{L}_{\text{high}}$ is now played by \mathcal{L}_* and the role of β is played by $\gamma_1 < 1$. In this way, the interpretation of the three panels in

Figure 3 is straightforward. As in the previous case, the high-energy exponential drop in the emissivity is due to the assumed maximum energy of protons in the accelerator.

3.2. Diffuse proton flux

Here we focus on the spectrum of protons at the Earth, when the source spectrum is computed accounting for self-confinement, as discussed above. The propagated flux of protons at $z = 0$ can be calculated following Berezinsky et al. (2006) and it reads:

$$J_p(E) = \frac{c}{4\pi} \int_0^{z_{\max}} dz \left| \frac{dt}{dz} \right| Q_p(E_g(E, z), z) \frac{dE_g(E, z)}{dE}, \quad (19)$$

where $\left| \frac{dt}{dz} \right| = H^{-1}(z)/(1+z)$, and the Jacobian $\frac{dE_g}{dE}$ is determined by the energy losses suffered by the protons during transport. We include pair production and photo-pion production on the Cosmic Microwave Background (CMB) radiation field as channels of energy losses and we compute the corresponding energy loss rates as functions of both energy and redshift by interpolating numerical tables generated using the latest release of the SimProp code (Aloisio et al. 2017). The adopted cosmology is the Planck Λ CDM model, with $h = 0.67$, $\Omega_m = 0.32$, and $\Omega_\Lambda = 0.68$ (Planck Collaboration et al. 2016).

3.3. Diffuse Neutrinos from UHECR Sources

In the standard scenario, UHECRs are promptly injected by sources into the IGM and propagate over cosmological distances. During their journey, interactions with background radiation fields generate a cosmogenic neutrino flux, which is directly tied to the flux of protons reaching the Earth.

In contrast, the scenario discussed in this work (like other scenarios involving near-source confinement (Unger et al. 2015; Muzio et al. 2022)) introduces an additional contribution to the diffuse neutrino background. This contribution arises from UHECRs that are unable to escape their near-source regions. In our framework, protons confined within the source environment cannot propagate into the IGM but may still produce neutrinos via photopion production.

Due to the relatively low maximum energies allowed by current mass composition measurements, most of these interactions occur with the Extragalactic Background Light (EBL) rather than with the CMB alone. For the EBL, we adopt the most recent determination provided by Saldana-Lopez et al. (2021). While the local EBL near sources could, in principle, exceed the average EBL, we neglect this effect here, as it strongly depends on the specific type of source under consideration.

Below, we describe the calculation of the neutrino flux produced by confined UHECRs, J_ν^{conf} , and compare it to the purely cosmogenic neutrino flux, J_ν^{cosmo} , which arises from UHECRs that successfully escape the near-source regions.

In the calculations of the effect of photopion production, we made use of the parametrization of the differential cross section described in Kelner & Aharonian (2010), which is obtained by fitting the energy distribution of the photopion interactions resulting from particle physics simulations performed with SOPHIA (Mücke et al. 2000). The energy distribution of the outgoing neutrinos is parametrized in terms of the fraction of energy of the impinging proton taken by the emitted neutrino, $x = E_\nu/E_p$. Using the same formalism adopted in Kelner & Aharonian (2010), the number of neutrinos produced per unit time and energy in the entire volume defined by

the flux tube around a source is given by:

$$q_\nu^{\text{conf}}(E_\nu, z) = \int_{E_p} \frac{dE_p}{E_p} N_p(E_p, t_{\text{age}}) \mathcal{R}(E_p, E_\nu, z), \quad (20)$$

where $N_p(E, t)$ is the number of protons with energy E confined within the flux tube at the time t , and $\mathcal{R}(E_p, E_\nu, z)$ is the production rate of neutrinos with energy E_ν from protons with energy E_p interacting with the background photons at redshift z . The production rate is defined using the parametrized cross-section as:

$$\mathcal{R}(E_p, E_\nu, z) = c \int_{\epsilon_{\text{th}}(E_p)} d\epsilon n_\gamma(\epsilon, z) \frac{d\sigma}{dx}(E_p, E_\nu, \epsilon), \quad (21)$$

where $\epsilon_{\text{th}}(E_p)$ identifies the threshold energy for the photopion interaction. To estimate the number of protons confined within the flux tube, we consider a continuous injection of protons from the source at a rate $q(E)$ and continuous escape from the flux tube at a rate defined by Equation (10):

$$\frac{\partial N_p(E, t)}{\partial t} = -\frac{N_p(E, t)}{\tau_{\text{esc}}(E)} + q(E). \quad (22)$$

The solution at $t = t_{\text{age}}$ holds:

$$N_p(E_p, t_{\text{age}}) = q(E_p) \tau_{\text{esc}}(E_p) \left[1 - e^{-\frac{t_{\text{age}}}{\tau_{\text{esc}}(E_p)}} \right], \quad (23)$$

which depends non trivially on the source luminosity through the protons escape time. The cosmological neutrino emissivity from confined protons is obtained by summing over the contribution of all the sources:

$$Q_\nu^{\text{conf}}(E_\nu, z) = \int d\mathcal{L}_p \Phi(\mathcal{L}_p, z) q_\nu^{\text{conf}}(E_\nu, \mathcal{L}_p, z), \quad (24)$$

Finally, the neutrino flux at Earth is obtained by solving the cosmological transport equation:

$$J_\nu^{\text{conf}}(E_\nu) = \frac{c}{4\pi} \int_0^{z_{\max}} dz \left| \frac{dt}{dz} \right| Q_\nu^{\text{conf}}(E_\nu(1+z), z) (1+z). \quad (25)$$

On the other hand, the flux of *cosmogenic* neutrinos is generated by unconfined protons propagating over cosmological distances. The proton spectral density at arbitrary redshift is determined in a way similar to Berezinsky et al. (2006):

$$n_p(E, z) = \int_z^{z_{\max}} dz_g \left| \frac{dt}{dz_g} \right| Q_p(E_g(E, z, z_g), z_g) \frac{dE_g(E, z, z_g)}{dE}. \quad (26)$$

Hence, the cosmogenic neutrino emissivity reads:

$$Q_\nu^{\text{cosmo}}(E_\nu, z) = \int_{E_p} \frac{dE_p}{E_p} n_p(E_p, z) \mathcal{R}(E_p, E_\nu, z), \quad (27)$$

and the diffuse cosmogenic neutrino flux at Earth is calculated as in Eq. (25):

$$J_\nu^{\text{cosmo}}(E_\nu) = \frac{c}{4\pi} \int_0^{z_{\max}} dz \left| \frac{dt}{dz} \right| Q_\nu^{\text{cosmo}}(E_\nu(1+z), z) (1+z). \quad (28)$$

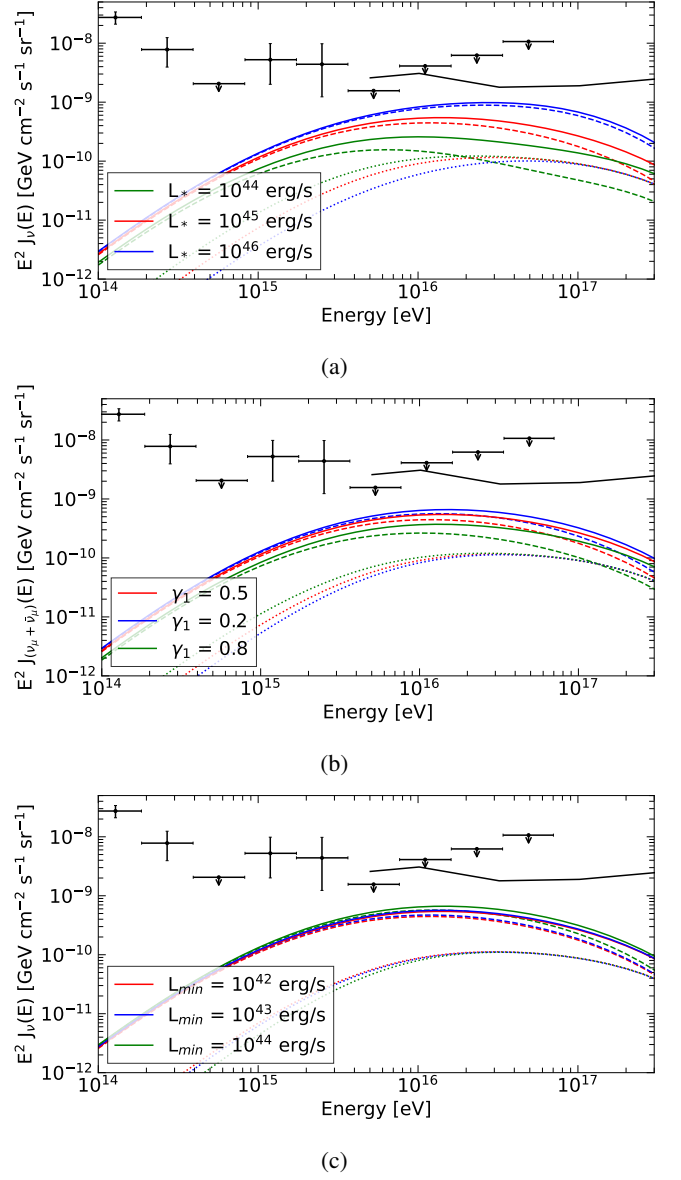
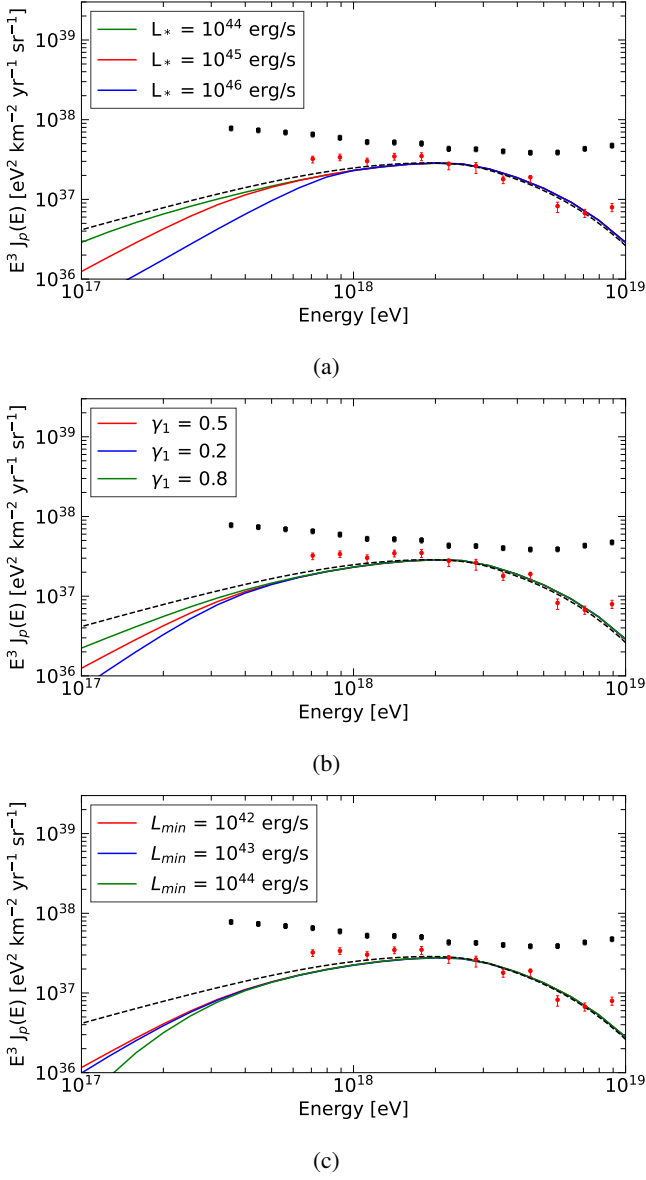


Fig. 4: Cosmic rays intensity at Earth. Top panel: different positioning of \mathcal{L}_* , with $\gamma_1 = 0.5$. Central panel: different slope, with the positioning of the break fixed at $\mathcal{L}_* = 10^{45}$ erg/s. Bottom panel: different choices of \mathcal{L}_{\min} , with $\mathcal{L}_* = 10^{45}$ erg/s and $\gamma_1 = 0.5$. $\gamma_2 = 2.5$ in all the cases. The all particle spectrum [Abreu et al. \(2021\)](#); [Aab et al. \(2020\)](#) and the proton spectrum obtained by adopting the mass fraction computed in [Aab et al. \(2016\)](#); [Aab et al. \(2014\)](#); [Aab et al. \(2014\)](#) using EPOS-LHC ([Pierog et al. 2015](#)) are shown with black squares and red circles, respectively. As a comparison, the same result is shown for an injection $Q_{src}(E) \propto E^{-2}$ (black dashed).

3.4. Comparison with observations

The flux of CR protons resulting from sources distributed with a luminosity function is shown in Figure 4, together with the all-particle spectrum measured by Auger ([Abreu et al. 2021](#); [Aab et al. 2020](#)) and the proton spectrum obtained by adopting the mass fraction computed in [Aab et al. \(2016\)](#); [Aab et al. \(2014\)](#); [Aab et al. \(2014\)](#) using EPOS-LHC ([Pierog et al. 2015](#)). The parameters defining the luminosity function for all the tested cases are listed in Table 1.

Fig. 5: Total diffuse neutrino flux at Earth (solid), coming from confined protons (dashed lines) and diffused ones (dotted lines). Top panel: different positioning of \mathcal{L}_* , with $\gamma_1 = 0.5$. Central panel: different slope, with the positioning of the break fixed at $\mathcal{L}_* = 10^{45}$ erg/s. Bottom panel: different choices of \mathcal{L}_{\min} , with $\mathcal{L}_* = 10^{45}$ erg/s and $\gamma_1 = 0.5$. $\gamma_2 = 2.5$ in all the cases. Measurements (black dots) and upper limits (black line and arrows) obtained by the Ice Cube Observatory [Aartsen et al. \(2013\)](#); [Kopper \(2017\)](#); [Abbasi et al. \(2025\)](#) are shown as a comparison.

The three panels refer to the same cases illustrated in Figure 3, and the normalization constant of the LF is chosen not to overshoot the proton spectrum measured by the Auger in the ankle region. As can be inferred from the comparison with an injection spectrum of E^{-2} (black-dashed), the confinement mechanism we have proposed is not necessary to explain the fraction of protons around 10^{18} eV, whereas it may be relevant for the cosmic ray spectrum above the ankle, where the inferred mass composition is increasingly heavier and the required spectral index at the escape from the source is unusually hard ([Abdul Halim et al. 2023](#)). However, the possibility that the

sources of the highest-energy cosmic rays also accelerate protons, although in a smaller fraction compared to heavier nuclei, cannot be excluded (Muzio et al. 2024). Moreover, in such a scenario, interactions within the confinement region lead to the production of secondary protons (Unger et al. 2015).

We then use the proton flux constrained by Auger data to derive an estimate of the contribution to the diffuse neutrino flux of these sources, provided the proposed mechanism is in place. In doing so, we assume that the maximum proton content allowed for the UHECR population that dominates above the ankle is restricted by the proton fraction measured by Auger, as in Figure 4.

The two contributions, J_{ν}^{cosmo} and J_{ν}^{conf} , are shown in Figure 5 for the same cases illustrated in Figure 4, with the same choice of the normalization constant. The neutrino flux produced by confined protons exceeds the cosmogenic one in the (1-100) PeV energy range. However, the total neutrino flux remains compatible with the upper limits posed by the Ice Cube experiment (Kopper 2017; Abbasi et al. 2025) even for the maximal choice about the proton flux, as discussed before.

A detailed study and comparison with the spectrum and mass composition as measured by Auger, including the nuclei and the related interactions inside the confinement environment, will be fully addressed in a forthcoming work.

4. Discussion and conclusions

The Auger data on the UHECR spectrum and mass composition unequivocally indicate that the dominant population of sources above the ankle (Abdul Halim et al. 2023) must inject a spectrum with a remarkably hard shape, and maximum energy in the range of a few EeV. Here, the term sources refers to astrophysical objects that may either host the real accelerators or act as storage environments for cosmic rays. This distinction is well illustrated by clusters of galaxies, which have long been recognized as natural reservoirs for cosmic rays over cosmological timescales (Berezinsky et al. 1997; Ensslin et al. 1997). Within such clusters, cosmic rays may be accelerated either by shocks in the intracluster medium or by individual galaxies. For cosmic rays with energies \lesssim PeV, the confinement time often exceeds the age of the universe, leading to a natural low-energy suppression that effectively hardens the spectrum. The Auger data suggest that such hardening likely occurs in the \lesssim EeV energy range.

This spectral hardening may also result from pronounced confinement processes similar to those inferred in galaxy clusters (Berezinsky et al. 1997; Ensslin et al. 1997). For instance, a combination of confinement and energy losses in specific sources (Unger et al. 2015; Muzio et al. 2022) or the magnetic horizon effect – where strong extragalactic magnetic fields create a low energy cutoff (Aloisio & Berezinsky 2004; Mollerach & Roulet 2013; Abdul Halim et al. 2024) – can mimic this phenomenon. However, the latter explanation requires relatively large magnetic fields that may only be marginally consistent with observational constraints, such as Faraday rotation measures, if such fields are ubiquitous.

We propose an alternative mechanism for this hardening: self-confinement driven by the excitation of plasma instabilities near powerful UHECR sources. When the energy density of escaping UHECRs exceeds the background magnetic field energy density, self-generated turbulence can significantly alter particle transport. In this work, we extend previous studies (Blasi et al. 2015) by exploring the environmental conditions under which self-confinement occurs at EeV energies. We calculate the resulting UHECR proton spectrum and diffuse neutrino flux in this framework.

Our results confirm that the scattering of UHECRs on self-generated magnetic perturbations leads to confinement timescales exceeding the source age for particles with \lesssim EeV energies. This effect imprints a low-energy suppression in the UHECR spectrum at Earth, influenced by the luminosity function of the sources.

The mechanism is particularly efficient if the source luminosity is of the order of $\sim 10^{45}$ erg/s and if the pre-existing IGMF is in the range $B_0 \sim 0.1 - 1$ nG, within a region of ~ 10 Mpc around the source. Notably, the non-resonant instability may still grow for lower values of B_0 , provided that particles down to \sim PeV contribute to the current (see Eq. (7)). Such conditions could naturally arise in environments like galaxy clusters, where the interplay between confinement and turbulence is prominent.

It is worth noticing that most potential UHECR accelerators, such as AGNs (Pimblet et al. 2012) or sources in starburst galaxies (Paccagnella et al. 2017), are indeed expected to reside within galaxy clusters. These regions are more likely to be magnetized due to the filamentary structure of the large-scale universe (Vernstrom et al. 2021; Carretti et al. 2022).

We calculated the UHECR proton flux from a cosmological population of sources with a typical luminosity function and compared our predictions with the Auger proton fraction (Abreu et al. 2021; Aab et al. 2020, 2014; Aab et al. 2014; Aab et al. 2016) interpreted using the EPOS-LHC hadronic interaction model (Pierog et al. 2015). Our results predict an excess of neutrino production in the near-source regions due to self-confinement of UHECRs with $E \lesssim 1$ EeV, compared to the cosmogenic neutrino flux from intergalactic space. However, the total neutrino flux remains consistent with current observational upper limits (Kopper 2017; Abbasi et al. 2025).

Finally, our model predicts that powerful UHECR sources should be surrounded by regions extending tens of Mpc, with turbulent magnetic fields reaching nG levels due to the saturation of the non-resonant instability. Observations of X-ray and radio emissions already suggest the presence of magnetized structures connecting galaxy clusters (Vernstrom et al. 2021), with average magnetic fields of 30–50 nG on scales $\gtrsim 3$ Mpc. Faraday rotation measures, which are sensitive to the mean magnetic field direction, impose upper limits on large-scale fields at the level of a few nG (O’Sullivan et al. 2020). However, these limits scale linearly with the assumed electron density, implying that magnetic fields in overdense regions, such as filaments, could be at least an order of magnitude larger.

The impact of amplified magnetic fields on Faraday rotation remains challenging to quantify, as it depends on the source luminosity function. The average rotation measure (RM) can be estimated as $\text{RM} \sim f^{1/2} n_e \langle \delta B \rangle$ (Amaral et al. 2021), where $\langle \delta B \rangle$ is the average amplified field strength weighted by the source luminosity function, n_e is the mean electron density and f is the filling factor, determined by the product of the source density and the volume of a single flux tube.

Assuming the same electron density as in Amaral et al. (2021), $n_e \simeq 10^{-5} \text{ cm}^{-3}$, we estimate $\text{RM} \lesssim 10^{-9} \mu\text{G cm}^{-3}$, roughly an order of magnitude smaller than the limits of the residual rotation measure limits reported in Amaral et al. (2021). Values of the averaged amplified field, filling factor, and RM are reported in table 1 for all the tested cases.

Acknowledgements. This work was partially funded by the European Union - NextGenerationEU under the MUR National Innovation Ecosystem grant ECS00000041 - VITALITY/ASTRA - CUP D13C21000430001. The work of PB was also partially funded by the European Union - Next Generation EU, through PRIN-MUR 2022TJW4EJ.

Table 1: Values of the normalization constant A of the tested luminosity functions, the resulting density of sources able to produce the NRSI $n(\mathcal{L}_{\min})$, the averaged amplified magnetic field $\langle B \rangle$, the volume fraction occupied by these sources f , and the estimate of the effect on the Faraday Rotation from the magnetized cocoons, RM. The luminosity functions extends up to $\mathcal{L}_{\text{high}} = 10^{48}$ erg/s, with a faint end slope $\gamma_2 = 2.5$, in all cases.

Different $\mathcal{L}_* - \mathcal{L}_{\text{low}} = 10^{40}$ erg/s - $\gamma_1 = 0.5$			
\mathcal{L}_* [erg/s]	10^{44}	10^{45}	10^{46}
A [Mpc $^{-3}$]	2.2×10^{-6}	2.2×10^{-7}	2.2×10^{-8}
$n(\mathcal{L}_{\min})$ [Mpc $^{-3}$]	1.3×10^{-5}	4.7×10^{-6}	1.5×10^{-6}
$\langle B \rangle$ [nG]	2.4	3.4	4.4
f	8.3×10^{-4}	2.9×10^{-4}	9.5×10^{-5}
RM [$\mu\text{G cm}^{-3}$]	6.8×10^{-10}	5.8×10^{-10}	4.3×10^{-10}
Different $\gamma_1 - \mathcal{L}_* = 10^{45}$ erg/s - $\mathcal{L}_{\text{low}} = 10^{40}$ erg/s			
γ_1	0.2	0.5	0.8
A [Mpc $^{-3}$]	3.2×10^{-7}	2.2×10^{-7}	1.1×10^{-7}
$n(\mathcal{L}_{\min})$ [Mpc $^{-3}$]	1.8×10^{-6}	4.7×10^{-6}	1.0×10^{-5}
$\langle B \rangle$ [nG]	5.7	3.4	2.3
f	1.1×10^{-4}	2.9×10^{-4}	6.4×10^{-4}
RM [$\mu\text{G cm}^{-3}$]	6.1×10^{-10}	5.8×10^{-10}	5.8×10^{-10}
Different $\mathcal{L}_{\text{low}} - \mathcal{L}_* = 10^{45}$ erg/s - $\gamma_1 = 0.5$			
\mathcal{L}_{low} [erg/s]	10^{42}	10^{43}	10^{44}
A [Mpc $^{-3}$]	2.2×10^{-7}	2.3×10^{-7}	3.0×10^{-7}
$n(\mathcal{L}_{\min})$ [Mpc $^{-3}$]	5.9×10^{-6}	1.8×10^{-6}	5.4×10^{-7}
$\langle B \rangle$ [nG]	2.7	6.6	14.2
f	3.7×10^{-4}	1.1×10^{-4}	3.4×10^{-5}
RM [$\mu\text{G cm}^{-3}$]	5.2×10^{-10}	7.0×10^{-10}	8.2×10^{-10}

References

Aab, A., Abreu, P., Aglietta, M., et al. 2016, Physics Letters B, 762, 288
Aab, A., Abreu, P., Aglietta, M., et al. 2014, Phys. Rev. D, 90, 122006
Aab, A., Abreu, P., Aglietta, M., et al. 2014, Phys. Rev. D, 90, 122005
Aab, A., Abreu, P., Aglietta, M., et al. 2020, Phys. Rev. D, 102, 062005
Aab, A., Abreu, P., Aglietta, M., et al. 2017, Journal of Cosmology and Astroparticle Physics, 2017, 038
Aartsen, M. G., Abbasi, R., Abdou, Y., et al. 2013, Physical Review Letters, 111
Aartsen, M. G., Ackermann, M., Adams, J., et al. 2019, Phys. Rev. D, 100, 082002
Abbasi, R. et al. 2025, arXiv [arXiv:2502.01963]
Abdul Halim, A., Abreu, P., Aglietta, M., et al. 2024, Journal of Cosmology and Astroparticle Physics, 2024, 094
Abdul Halim, A., Abreu, P., Aglietta, M., et al. 2023, Journal of Cosmology and Astroparticle Physics, 2023, 024
Abreu, P., Aglietta, M., Albury, J. M., et al. 2021, The European Physical Journal C, 81, 1
Ajello, M., Costamante, L., Sambruna, R. M., et al. 2009, The Astrophysical Journal, 699, 603
Ajello, M., Shaw, M. S., Romani, R. W., et al. 2012, The Astrophysical Journal, 751, 108
Aloisio, R. & Berezhinsky, V. 2004, The Astrophysical Journal, 612, 900

Aloisio, R., Boncioli, D., di Matteo, A., et al. 2017, Journal of Cosmology and Astroparticle Physics, 2017, 009
Amaral, A. D., Vernstrom, T., & Gaensler, B. M. 2021, Monthly Notices of the Royal Astronomical Society, 503, 2913
Amato, E. & Blasi, P. 2009, Monthly Notices of the Royal Astronomical Society, 392, 1591
Arons, J. 2003, ApJ, 589, 871
Asano, K. & Mészáros, P. 2016, Phys. Rev. D, 94, 023005
Bell, A. R. 2004, MNRAS, 353, 550
Berezinsky, V., Gazizov, A., & Grigorieva, S. 2006, Phys. Rev. D, 74, 043005
Berezinsky, V. S., Blasi, P., & Ptuskin, V. S. 1997, The Astrophysical Journal, 487, 529
Bergman, D. 2006, Journal of Physics: Conference Series, 47, 154
Blandford, R. & Eichler, D. 1987, Physics Reports, 154, 1
Blandford, R. D. & Ostriker, J. P. 1978, ApJ, 221, L29
Blasi, P. & Amato, E. 2019, Phys. Rev. Lett., 122, 051101
Blasi, P., Amato, E., & D'Angelo, M. 2015, Phys. Rev. Lett., 115, 121101
Blasi, P., Epstein, R. I., & Olinto, A. V. 2000, ApJ, 533, L123
Burlon, D., Ajello, M., Greiner, J., et al. 2011, The Astrophysical Journal, 728, 58
Carretti, E., O'Sullivan, S. P., Vacca, V., et al. 2022, Monthly Notices of the Royal Astronomical Society, 518, 2273
Ensslin, T. A., Biermann, P. L., Kronberg, P. P., & Wu, X.-P. 1997, ApJ, 477, 560
Fotopoulou, S., Buchner, J., Georgantopoulos, I., et al. 2016, A&A, 587, A142
Gargatè, L., Fonseca, R. A., Niemiec, J., et al. 2010, The Astrophysical Journal Letters, 711, L127
Kang, D. 2023, PoS, ICRC2023, 307
Kelner, S. R. & Aharonian, F. A. 2010, Phys. Rev. D, 82, 099901
Kopper, C. 2017, PoS, ICRC2017, 981
Kotera, K., Amato, E., & Blasi, P. 2015, J. Cosmology Astropart. Phys., 2015, 026
Mollerach, S. & Roulet, E. 2013, Journal of Cosmology and Astroparticle Physics, 2013, 013
Mücke, A., Engel, R., Rachen, J. P., Protheroe, R. J., & Stanev, T. 2000, Computer Physics Communications, 124, 290
Muzio, M. S., Anchordoqui, L. A., & Unger, M. 2024, A Peters cycle at the end of the cosmic ray spectrum?
Muzio, M. S., Farrar, G. R., & Unger, M. 2022, Phys. Rev. D, 105, 023022
O'Sullivan, S. P., Brüggemann, M., Vazza, F., et al. 2020, Monthly Notices of the Royal Astronomical Society, 495, 2607
Paccagnella, A., Vulcani, B., Poggianti, B. M., et al. 2017, The Astrophysical Journal, 838, 148
Pierog, T., Karpenko, I., & Katzy, J. M. e. a. 2015, Physical Review C, 92, 034906
Pimblett, K. A., Shabala, S. S., Haines, C. P., Fraser-McKelvie, A., & Floyd, D. J. E. 2012, Monthly Notices of the Royal Astronomical Society, 429, 1827
Planck Collaboration, Ade, P. A. R., Aghanim, N., et al. 2016, A&A, 594, A13
Qu, Y., Zeng, H., & Yan, D. 2019, Monthly Notices of the Royal Astronomical Society, 490, 758
Riquelme, M. A. & Spitkovsky, A. 2009, The Astrophysical Journal, 694, 626
Saldana-Lopez, A., Domínguez, A., Pérez-González, P. G., et al. 2021, Monthly Notices of the Royal Astronomical Society, 507, 5144
Schroer, B., Pezzi, O., Caprioli, D., Haggerty, C., & Blasi, P. 2021, ApJ, 914, L13
Schroer, B., Pezzi, O., Caprioli, D., Haggerty, C. C., & Blasi, P. 2022, MNRAS, 512, 233
Shinozaki, K. & Teshima, M. 2004, Nuclear Physics B - Proceedings Supplements, 136, 18
Sironi, L., Keshet, U., & Lemoine, M. 2015, Space Sci. Rev., 191, 519
Subedi, P., Sonsrrette, W., Blasi, P., et al. 2017, ApJ, 837, 140
Unger, M., Farrar, G. R., & Anchordoqui, L. A. 2015, Phys. Rev. D, 92, 123001
Vernstrom, T., Heald, G., Vazza, F., et al. 2021, Monthly Notices of the Royal Astronomical Society, 505, 4178
Zhang, H., Sironi, L., Giannios, D., & Petropoulou, M. 2023, ApJ, 956, L36
Zweibel, E. G. & Everett, J. E. 2010, The Astrophysical Journal, 709, 1412